Three-dimensional analysis of Eu dopant atoms in Ca-α-SiAlON via through-focus HAADF-STEM imaging

Genki Saito [a], Fuuta Yamaki [a], Yuji Kunisada [a], Norihito Sakaguchi [a], Tomohiro Akiyama [a]*

[a] Center for Advanced Research of Energy and Materials, Hokkaido University, Kita 13 Nishi 8, Kitaku, Sapporo 060-8628, Japan

[*]Corresponding author: Tel.: +81 11 706 6766; E-mail address: genki@eng.hokudai.ac.jp (G. Saito)

Keywords: dopant distribution; through-focus; STEM; HAADF; phosphor; SiAlON; image simulation; aberration correction

Abstract[1]

Three-dimensional (3D) distributional analysis of individual dopant atoms in materials is important to development of optical, electronic, and magnetic materials. In this study, we adopted through-focus high-angle annular dark-field (HAADF) imaging for 3D distributional analysis of Eu dopant atoms in Ca-α-SiAlON phosphors. In this context, the effects of convergence semi-angle and Eu z-position on the HAADF image contrast were investigated. Multi-slice image simulation revealed that the contrast of the dopant site was sensitive to change of the defocus level. When the defocus level matched the depth position of a Eu atom, the contrast intensity was significantly increased. The large convergence semi-angle greatly increased the depth resolution because the electron beam tends spread instead of channeling along the atomic columns. Through-focus HAADF-STEM imaging was used to analyze the Eu atom distribution surrounding 10 nm cubes with defocus steps of 0.68 nm each. The contrast depth profile recorded with a narrow step width clearly analyzed the possible depth positions of Eu atoms. The radial distribution function obtained for the Eu dopants was analyzed using an atomic distribution model that was based on the assumption of random distribution. The result suggested that the Ca concentration did not affect the Eu distribution. The decreased fraction of neighboring Eu atoms along z-direction might be caused by the enhanced short-range Coulomb-like repulsive forces along the z-direction.

[1] Abbreviations: LED: light-emitting diode; HAADF-STEM: High-angle annular dark-field scanning transmission electron microscopy; TDS: thermal diffuse scattering; FWHM: full width at half maximum.

1. Introduction

It is well known that dopant atoms in host materials can affect their optical, electrical, and magnetic properties. In the field of white light-emitting diodes (LEDs), rare earth doped phosphors including Ce- or Eu-doped YAG [1], SiAlON [2], $CaAlSiN_3$ [3], and Ca_2SiO_4 [4] have been used to adjust complex LED white light. In this context, analysis of dopant concentration, doping site, and three-dimensional (3D) distribution is very important to understanding and controlling luminescence properties. Of the phosphors currently available, Eu-doped Ca-α-SiAlON is attractive because of its excellent properties including small thermal quenching and high quantum efficiency. The basic structure of α-SiAlON follows that of α-Si_3N_4, but Al and O atoms substitute for Si and N atoms respectively, resulting in solid solution crystals. Because of Al^{3+} and O^{2-} ions, dopant atoms such as Y, Ca, Sr, and Eu can insert into the interstitial sites in α-SiAlON [5, 6]. Eu-doped Ca-α-SiAlON can be described as $Ca_xSi_{12-(m+n)}Al_{m+n}O_nN_{16-n}:Eu_y$ ($m = 2x + 2y$, $m = 2n$). In following with this equation, the concentrations of Al and O were increased alongside the dopant concentration to maintain charge neutrality. According to the literature [2, 7, 8], the optimum Eu (y) content for higher luminescence ranges from 0.05 to 0.075. Ca content (x) also affects the luminescence intensity and wavelength. In particular, a high m value leads to increases in intensity and a red shift in the emission wavelength [9]. However, the reason for increased luminescence is still not clear.

Investigation of the 3D distributions of doped rare earth atoms is crucial for a deeper understanding of their luminescence properties because energy transfer can occur between two nearby dopant atoms, which results in a decrease in light emission efficiency [10]. Conventionally, X-ray and neutron diffractometry have been used to identify doping sites [11, 12]. However, it has been difficult to determine the 3D distribution of dopant atoms using these methods. High-angle annular dark-field scanning transmission electron microscopy (HAADF-STEM) is very useful for direct imaging of single, heavy dopants within a host

material. The image contrast of HAADF-STEM is proportional to the atomic number ($\propto Z^{1.6-2.0}$) because thermal diffuse scattering (TDS) is dominant in high angle electron scattering. Therefore, HAADF-STEM has been used for analyzing column-by-column atomic structures such as Si and InGaN semiconductors [13-16], oxides [17-19], nitrides [20-24], and so on. Recently, electron tomography [25-29] and slight tilting [30] have been proposed to determine 3D single-atom spatial distributions. These methods are effective for analysis of thin materials such as nanoparticles and nanowires. However, they are not suitable when electron channeling behavior changes drastically depending on incident direction. For thorough analysis of the observed STEM image, image simulation, in which scattering and channeling behaviors of the electron probe are predicted quantitatively, is essential. HAADF-STEM imaging by counting electrons with an accurately calibrated ADF detector using frozen phonon calculations has also been proposed [31, 32] and has perfectly clarified the 3D distribution of Ce dopants in wurtzite-type AlN [33]. The quantitative STEM was also applied for 3D imaging of Gd dopant atoms in $SrTiO_3$ [34, 35]. However, these quantitative methods are considered unsuitable for analyzing Eu dopant atoms in Ca-α-SiAlON because when Eu dopant atoms are doped into the Ca column, in which the occupancy of Ca atoms is approximately 0.3-0.6, the Ca concentrations and arrangements vary in each dopant column. These different arrangements of Ca atoms strongly affect the column intensity [36], causing difficulty in the quantitative analysis of Eu atoms in Ca columns (detailed calculation results are supplied in S1 in the Supplementary materials). To solve this problem, we focused on depth sectioning via through-focus or focal-series imaging [37-40]. The advantages of this method are its simple procedure and the lack of need for special customization or complete calibration. Spherical aberration-corrected electron probes improve not only the transverse resolution, but also the depth resolution [41]. Therefore, contrast enhancement is expected for elements around the focal position. Through-focus imaging enables the analysis of individual Eu atoms present within the dopant column at different Ca concentrations and in different

arrangements. However, the depth resolution is not still high, and is insufficient for the atomic scale analysis.

In the present study, we propose through-focus HAADF-STEM imaging for 3D distributional analysis of Eu dopant atoms in Ca-α-SiAlON phosphors. To achieve high depth resolution, the defocus was changed by narrow steps. The contrast profile obtained for various depths at each dopant column was compared to simulation results to determine the depth position. Although the depth resolution is limited, the contrast depth profile recorded by through-focus imaging with narrow step widths can determine the possible depth positions of Eu atoms. From the 3D distribution of Eu atoms, the radial distribution function is analyzed with different concentrations of Ca. Finally, we discuss the atomic distribution model of Eu atoms in Ca-α-SiAlON.

2. Experimental

$Ca_xSi_{12-(m+n)}Al_{m+n}O_nN_{16-n}:Eu_y$ (x = 0.6 and 1.2, y = 0.06; m = 2x + 2y, m = 2n) was prepared via combustion synthesis [42, 43]. The raw materials included Si (>99.9 % purity, 5 μm), Al (99.9 % purity, 3 μm), CaO (99.9 % purity), Eu_2O_3 (99.9 % purity), and α-Si_3N_4 (99.9 % purity, 0.5 μm) powders. The mixture was loaded into a porous alumina crucible. The combustion reaction was conducted under nitrogen (99.99 % purity), at a pressure of 0.8 MPa by passing current through a carbon foil. To prepare the TEM samples, the synthesized powder was mixed with fine copper powder (99.99 %, 1 μm) and hot-pressed at 300 °C for 1 hour. The composite disk of α-SiAlON and copper was sliced and mechanically polished down to a thickness of less than 20 μm, and then ion-milled with 5 ~ 1 kV Ar ions (PIPS model 691, Gatan Inc.). HAADF-STEM (Titan^3 G2 60-300, FEI Company) was performed at 300 kV. The inner collection semi-angle of the HAADF detector and the convergence semi-angle of the electron probe were 64 and 30 mrad, respectively. Through-focus HAADF-STEM imaging was performed near 10 nm cubes with a defocus step of 0.68 nm,

where the defocus steps were calibrated using high-precision z-displacement (detailed results are supplied in S5 of the Supplementary materials). When the STEM images were acquired, the image contrast was maintained to be linear for the detector signal without an automatic contrast or brightness adjustment. A non-saturation brightness level was selected. The drift of the through-focus images was corrected, and the column intensities of both experimentally obtained and calculated images were determined from the integrated intensity, where the diameter of the selected area was approximately 0.15 nm. The number of Eu atoms was determined from the shape and absolute intensity of the contrast profile. The Eu depth position was analyzed using the peak position of the profile. The HAADF-STEM images were also calculated with the Dr. Probe multi-slice image simulator [44], which uses the frozen phonon approximation to incorporate the influence of TDS. A parameterized scattering factor, which was reported by Weickenmeier and Kohl [45], was used as an atomic scattering factor because of its high accuracy at high angles. A frozen phonon calculation was performed by including random atom displacements to represent thermal atom vibrations. Based on the calculated number of pixels, approximately ten variants of frozen phonons were considered for one column, in which the atomic scattering factor was fixed to be 0.5 $Å^{-2}$ for every atom. According to the reciprocal of the number of supercells used, the resolution in reciprocal space was found to be 0.07 $Å^{-1}$. In these image simulations, we used a Gaussian function with a full width at half maximum of 0.04 nm for the electron probe intensity distribution. The defocus spread was set to 3 nm.

3. Results and discussion

Fig. 1(a) shows the atomic structure model of Eu-doped Ca-α-SiAlON along the [0001] direction. Ca and Eu atoms are located in the same column. When Ca content x = 0.6 and Eu content y = 0.06, the occupancies of Ca and Eu in one dopant column are 0.3 and 0.03, respectively. With an increase in x from 0.6 to 1.2, the amounts of Ca, Al and O increase and

the crystal lattice expands due to an increase in long Al-O bonds. The x value also affects the luminescence properties [8]. In this study, samples were synthesized with x = 0.6 and 1.2. X-ray diffractometry showed a lattice expansion with an increase in x, and an increase in luminescence properties at x = 1.2.

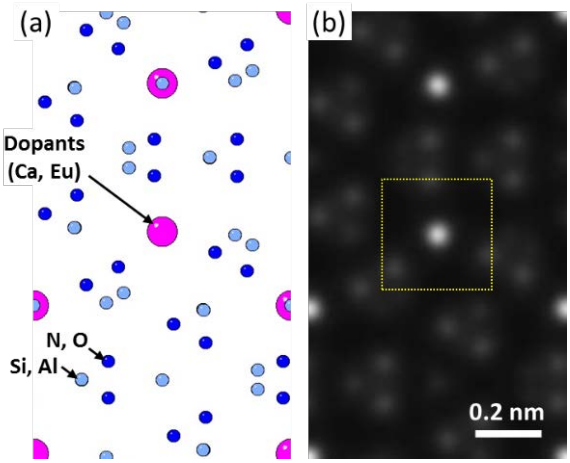

Fig. 1. (a) Atomic structure model of Eu-doped Ca-α-SiAlON, in the [0001] direction. (b) Multi-slice simulated image of Eu-doped Ca-α-SiAlON, in which one Eu atom is located at -5.48 nm along the z-direction and defocus is -5.52 nm (sample thickness: 20 nm, convergence semi-angle: 30 mrad).

For multi-slice image calculations, a supercell of Ca-α-SiAlON (x = 0.6) with a thickness of 20 nm was prepared. When the sample thickness was 20 nm, 36 atomic sites were present in one dopant column. The average numbers of Ca and Eu atoms expected are 10.8 and 1.08, respectively. These dopant atoms can be inserted interstitially. In the calculation, Ca atoms were uniformly arranged along the dopant column. Fig. 1(b) shows the simulated HAADF image of Ca-α-SiAlON, in which one Eu atom is located at -5.48 nm along the z-direction and the defocus was -5.52 nm (sample thickness: 20 nm, convergence semi-angle: 30 mrad). The simulated image is matched to the atomic structure shown in Fig. 1(a), and the brightest dots correspond to the dopant column because the atomic numbers of Ca and Eu are higher than those of Si and N. When the effects of convergence semi-angle and

Eu z-position on the contrast were investigated, the simulated area was limited to that near the dopant column in the dotted square in Fig. 1(b) in order to reduce the calculation time.

Through-focus images were calculated by changing the defocus from 0.00 to -16.10 nm using steps of 0.42 nm. This is the minimum step size supported by the STEM used in this study. Fig. 2(a) shows simulated images of Eu sites, where one Eu atom is located at a depth of -5.48 nm and 30 mrad was used as the convergence semi-angle. The contrast of the dopant site is sensitive to changes in defocus. When the defocus matches the depth of a Eu atom, the contrast increases significantly. This behavior can be explained by the shallow focus depth. Generally, focus depth decreases when the convergence semi-angle is increased. Therefore, a spherical aberration-corrected electron beam increases the spatial resolution, which enhances the information around the focal position [41]. Y. Oshima also reported the dependence of contrast on defocus using STEM imaging of As-doped silicon, in which the maximum intensity was obtained when the electron probe was focused within the 2.7 nm defocusing range of the doped atom [46].

The change in contrast of dopant columns with different levels of defocus is summarized in Figs. 2(b) and (c). Here, the plots show the contrast at each defocus level and the dotted lines are curves fit using the Lorentzian peak function. The Lorentzian peak function is more suitable for curve fitting than the Gaussian function because of its bell shape and much wider tails. The linear model with gradient was applied as a background. This relationship might be due to a decrease in beam intensity as defocus increases. In the present calculation, the convergence semi-angle was varied to 22, 30, and 45 mrad at a fixed Eu atom depth of -5.48 nm, as shown in Fig. 2(b). Table 1 summarizes the full width at half maximum (FWHM) and detected peak positions at different convergence semi-angles. When the convergence semi-angle is increased from 22 to 45 mrad, the FWHM of the peaks decreases from 9.26 to 1.85 nm and the accuracy of the Eu position detection is enhanced. This indicates that a large convergence semi-angle is effective for increasing the depth resolution because the electron

beam tends spread instead of channeling along the atomic columns. A convergence semi-angle of 30 mrad was used for real observations. This was an optimal value for high-resolution HAADF-STEM with the present STEM. The effect of Eu depth is also studied in Fig. 2(c), where Eu atoms are located at different depths of -2.06, -5.48, and -10.62 nm. The convergence semi-angle was assumed to be 30 mrad. Table 2 shows the FWHM of the intensity profile and the peak position, which indicate that the Eu depth position can be analyzed within the range of -2.06 to -10.62 nm. At a dopant depth of -2.06 nm, accuracy was reduced because of the asymmetric shape of the fitting curve.

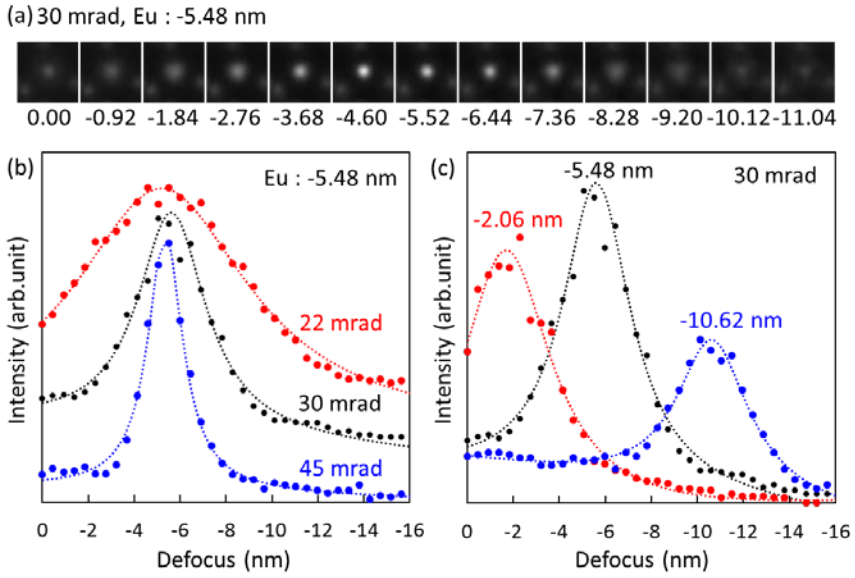

Fig. 2. (a) Simulated images of an Eu site with different levels of defocus from 0.00 to -11.04 nm. (b, c) defocus profiles of an Eu site evaluated via multi-slice simulation with different electron probe convergence semi-angles, and different depth positions of Eu atoms.

Table 1. FWHM and peak position at different convergence semi-angles with a dopant depth of -5.48 nm.

Converged semi-angle	22 mrad	30 mrad	45 mrad
FWHM (nm)	9.26	3.60	1.85
Peak position, z (nm)	-5.21	-5.63	-5.36
Error, Δz (nm)	0.27	0.15	0.12

Table 2. FWHM and peak position at different dopant depths, with a convergence semi-angle of 30 mrad.

Doped depth (nm)	-2.06	-5.48	-10.62
FWHM (nm)	4.81	3.60	3.80
Peak position (nm)	-1.68	-5.63	-10.66
Error, Δz (nm)	0.38	0.15	0.04

According to these simulated results, through-focus HAADF-STEM imaging shows the potential to analyze the depth position of an Eu atom. However, there are some important issues to consider. First, channeling sometimes affects the contrast, which makes position analysis more difficult. In the Ca-α-SiAlON structure, the channeling effect is not serious because of the low site occupancy of Ca and the large difference in atomic number between Ca (20) and Eu (63). We also investigated the effect of the Ca arrangement. The average occupancy of Ca atoms is approximately 0.3; however, some atomic columns can have a higher occupancy and others one should be lower occupancy. We calculated such variations in the Ca arrangement, as shown in S2 in the Supplementary materials. Although Ca segregation generates broad peaks in the contrast profiles, we can distinguish the presence of Eu atoms from Ca segregation because of the sharper, more intense peaks from the presence of Eu. In addition, we should discuss how to deal with cases where more than one Eu atom is located in the same column. Fig. 3 shows defocus profiles evaluated via multi-slice simulation with two Eu atoms located at different depths. When the Eu atoms are located at

depths of -5.48 and -10.62 nm, the multi-slice image simulation indicates that their contrast profile is nearly equal to the sum of each single atom profile shown in red and blue dotted lines in Fig. 3(a). Therefore, we can determine the depth positions of two Eu atoms located at the same column. However, when two Eu atoms are located within 2 nm of each other along the z-direction, it is difficult to determine their actual separation distance, as shown in Fig. 3(b). A larger convergence semi-angle is required to distinguish such a narrow distance. Although some issues exist, through-focus HAADF-STEM imaging shows the potential to analyze the Eu atom distribution in Ca-α-SiAlON. We have treated the matters discussed above with care when analyzing the HAADF-STEM images.

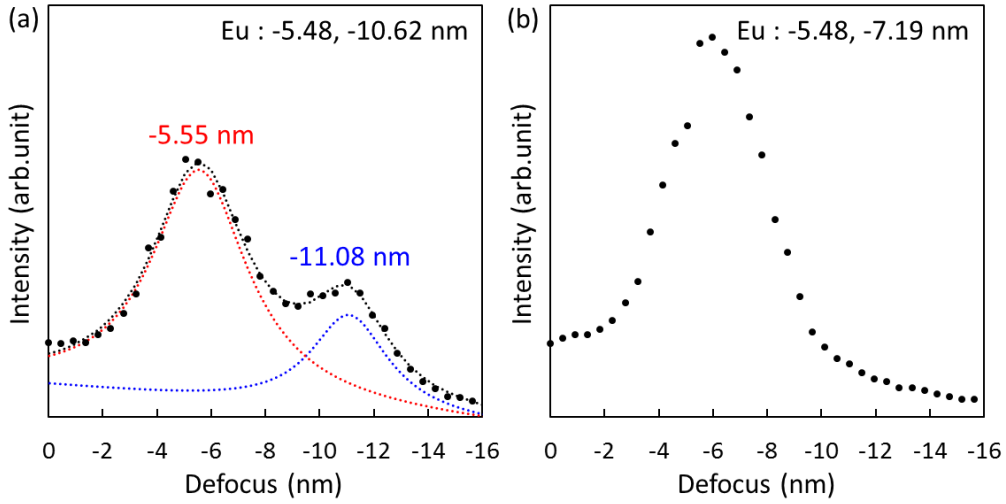

Fig. 3. Defocus profiles via multi-slice image simulation with two Eu atoms located at different depths of (a) -5.48 and -10.62 nm, and (b) -5.48 and -7.19 nm.

Through-focus HAADF-STEM imaging for synthesized particles was performed to a sample thickness of around 30 nm with defocus steps of 0.68 nm, a convergence semi-angle of 30 mrad, and an image resolution of 2048 × 2048 pixels. The sample thickness was estimated from the intensity ratio between two different Si columns (see S3 in the Supplementary materials). In the Ca-α-SiAlON structure, the Si column intensity depends on the sample thickness because of the unique electron channeling. According to a comparison between the calculated and experimental results, the sample thickness was approximately 30

nm. We also investigated the effect of the sample thickness on the contrast profile (S4 in the Supplementary materials). The results indicated that the sample thickness only slightly affected the contrast profile. Because the spherical-aberration-corrected electron probes with a convergence semi-angle of 30 mrad improves the depth resolution, contrast enhancement is expected for elements around the focal position, resulting in insensitivity to the sample thickness.

In the experiment, the defocus was varied from 0 to -20.3 nm, resulting in 30 through-focus images. After unification of the contrast range, an average image was generated from the 30 drift-corrected through-focus images. Figs. 4(a, b) show HAADF-STEM images of Eu-doped Ca-α-SiAlON (x=0.6) at different defocus levels and an average image generated from 30 individual images. The bright dots in these images correspond to the Ca and Eu dopant sites. Columns of Si (Al) and N (O) had relatively lower contrast due to having smaller atomic numbers than Ca and Eu. The brightness of the dopant sites varies with the atoms in each column. In addition, when Eu atoms are in a particular column, the contrast of this column increases and the defocus level with the highest intensity indicates the depth of the Eu atom. Here, some columns have higher contrast at every defocus level, which might suggest that they contain many Ca atoms. Eu is located in the same column as the Ca atoms, and the occupancy of Ca atoms is not 1.0. Therefore, the Ca concentration and arrangement can be changed at each column. The effect of such Ca arrangements has been illustrated in S2 in the Supplementary materials. Fig. 4(c) shows an enlargement of column c from Fig. 4(a) at each defocus level. The highest contrast is near -5.41 nm, which suggests that this is the location of the Eu atom. At defocus levels of over -10.7 nm, the contrast of column c decreases significantly due to the absence of nearby Eu atoms. From these results, it is clear that one image observed at a fixed defocus level does not supply information about Eu atoms located at different depths. To find all Eu atoms, though-focus imaging is required. To analyze the number and depths of Eu atoms, the

contrast profiles of each atomic column were carefully analyzed one-by-one using 30 recorded through-focus images. Finally, we determined the depth positions of the Eu atoms using the defocus with the highest contrast and profile shape.

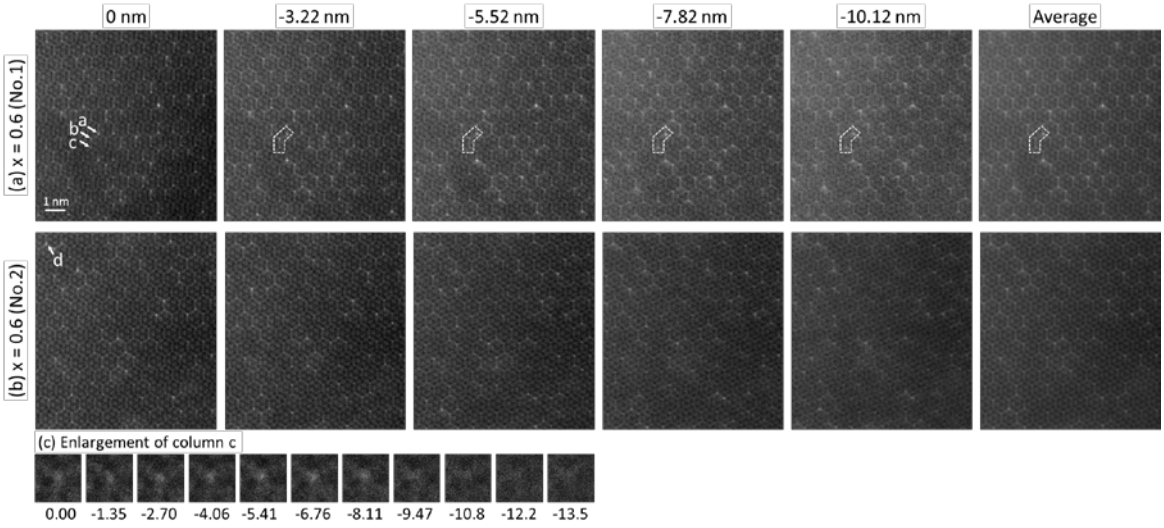

Fig. 4. HAADF-STEM images at different defocus values of Eu doped Ca-α-SiAlON of x = 0.6 No. 1 (a) and No. 2 (b) with averaged HAADF-STEM images, which are the averages of 30 images obtained at different defocus values. (c) Enlargement of column c in Fig. 4(a) at each defocus level (nm).

Fig. 5 shows the contrast profiles acquired from through-focus HAADF-STEM images. Figs. 5(a-d) correspond to the arrows in Fig. 4(a, b). From these profiles, we have determined the existence and depth of the Eu atoms. When analysing the contrast profile, the linear background model was applied as seen in Fig.S7 (a). The evaluated peak intensity was used for detecting Eu. The distribution of these peak intensities are summarized in Fig.S7 (b), in which two peaks correspond to Ca and Eu. When peak intensity was over 14, we judged that the Eu atom located at this column. In the practical analysis procedure, threshold of peak intensity was slightly reduced with an increase of defocus owing to the decreases in peak intensity as shown in the Fig. 2(c). In Fig. 5(a), the contrast gradually decreases without any significant peaks, which suggests the absence of Eu atoms in this column. The contrasts of

positions (b) and (c) have peaks which reveal the presence of Eu atoms in these columns. In these cases, -2.70 and -5.41 nm were identified as the depths of the Eu atoms. Two Eu atoms were also detected in one column, as shown in Fig. 5(d). The peak of column ‘c’ was broader than that of ‘b’. The image simulation shown in Fig. S2-2 in the Supplementary materials suggests that the peak broadening was enhanced with an increase in the depth position of Eu atoms. This phenomenon might have been induced by the scattering of the electron beam. The intensity profile of column ‘d’ exhibits a similar trend.

Two Eu atoms were also detected in one column, as shown in Fig. 5(d). The peak of column ‘c’ was broader than that of ‘b’. The image simulation shown in Fig. S2-2 in the Supplementary materials suggests that the peak broadening was enhanced with an increase in the depth position of Eu atoms. This phenomenon might have been induced by the scattering of the electron beam. The intensity profile of column ‘d’ exhibits a similar trend.

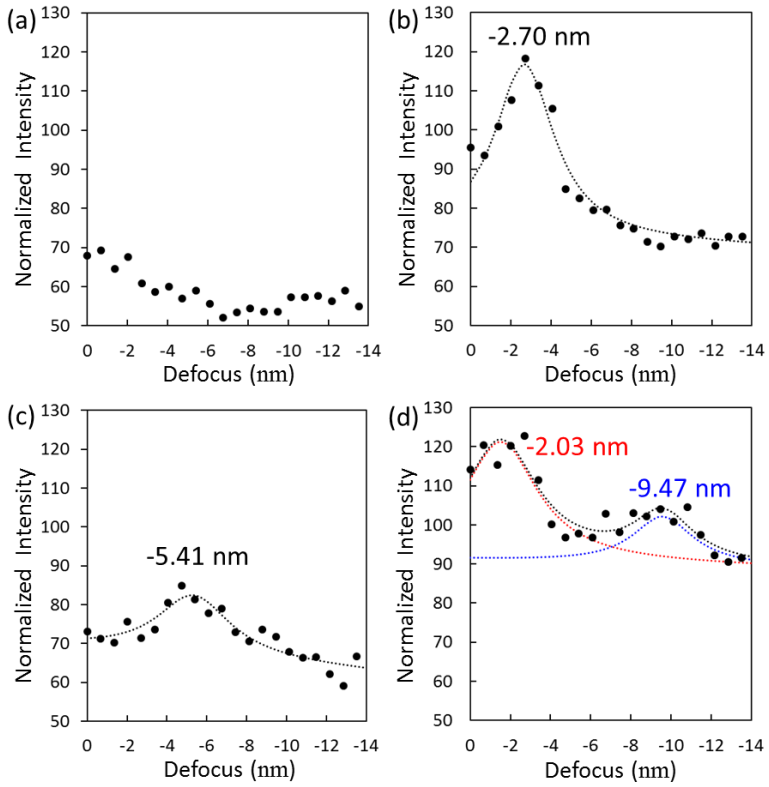

Fig. 5. Contrast profiles acquired from through-focus HAADF-STEM images of Eu-doped Ca-α-SiAlON (x=0.6), in which (a-d) correspond to the arrows in Figs. 4(a, b).

To analyze the dopant distribution in a statistically significant manner, three different areas were observed at each composition. In total, 2037 columns were analyzed and 768 Eu atoms were detected in 6 areas. Fig. 6 shows the resulting 3D distribution of Eu atoms. Segregation of Eu atoms is not clearly apparent from this distribution. The number density of the Eu atoms is summarized in Table 3; it was slightly lower than the theoretical Eu density of 0.20 nm^{-3}. The Eu atoms may not have been doped perfectly into the Ca column, and so some of them may have been segregated.

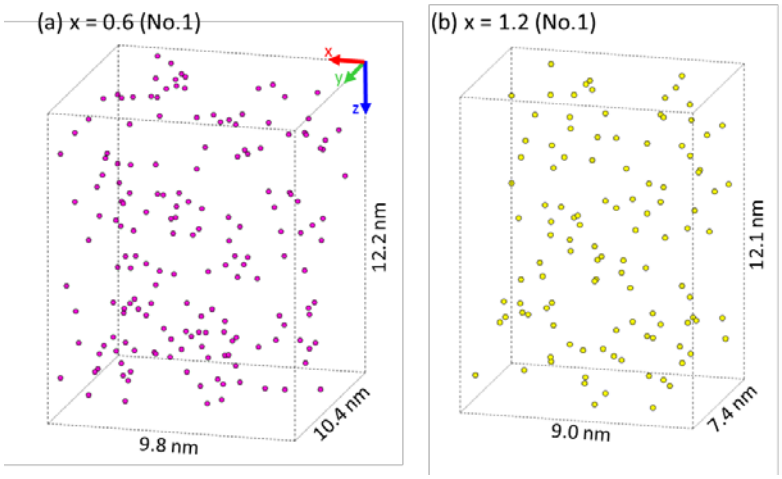

Fig. 6. 3D Eu atom distributions for (a) x=0.6 and (b) x=1.2.

Table 3. Number density of Eu atoms detected. Here, the theoretical density is 0.20 / nm^3.

	No. 1	No. 2	No. 3
x = 0.6	0.16 / nm^3	0.15 / nm^3	0.15 / nm^3
x = 1.2	0.15 / nm^3	0.17 / nm^3	0.14 / nm^3

We have evaluated the radial distribution function in order to characterize the distribution morphology of Eu atoms. Fig. 7(a) shows the configuration of Eu atoms in a unit structure. When one Eu atom is focused upon (see yellow atom), six Eu atoms labeled “1” are first neighbors and two Eu atoms labeled “2” are second neighbors. With the assumption of

100 % occupancy of Eu atoms, the radial distribution function can be represented by Fig. 7(a). In our through-focus imaging, the depth position was analyzed in steps of 0.68 nm, and thus the Eu atom configuration changes as shown in Fig. 7(b). Here, we define this analytically derived coordination system as “analyzed coordination system”. This analyzed coordination system (Fig. 7(b)) differs from the real coordination system (Fig. 7(a)) because the nearest distance between Eu atoms along the z-direction is 0.57 nm in the real system. Although the resulting radial distribution functions change between the two coordination systems, each peak corresponds as shown in the radial distribution function displayed in Fig. 7(b). For example, the distance of 2’ consists of 66.7 % of 2 and 33.3 % of 7 in the real coordination system (see Fig. S6 in the Supplementary materials). By evaluating the fraction at each distance, the simulated coordination system can be perfectly adjusted to match the real coordination system.

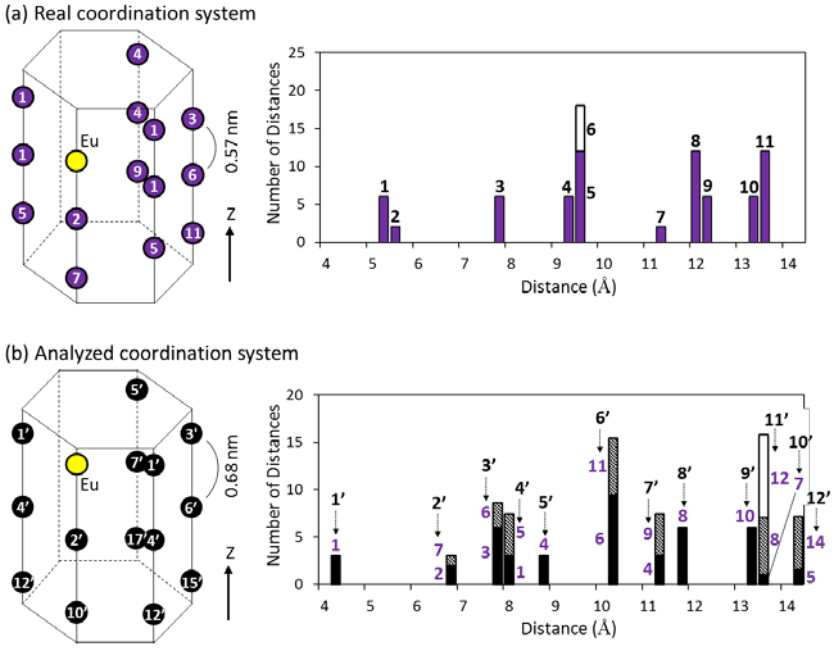

Fig. 7. (a) Real coordination system of Eu sites and (b) analyzed coordination system and its corresponding radial distribution functions.

Fig. 8 shows the analyzed and converted radial distribution functions for Eu atoms with different Ca concentrations. The converted radial distribution was obtained using the fraction at each distance, as discussed above. According to the two radial distribution functions, there is no significant difference between the distributions obtained at x=0.6 and x=1.2, which suggests that the concentration of Ca does not affect the Eu atom distribution. Figs. 8(a-3) and (b-3) show radial distribution functions from a random distribution model, which was calculated based on 3 % occupancy of Eu atoms. When Eu atom distribution is perfectly random, the radial distribution function must have a similar shape to that of 100 % occupancy, shown in Fig. 7. Except for first- and second-neighbor atoms, the distributions obtained for x = 0.6 and x = 1.2 match the random distribution model well. In addition, the fractions of a seventh-neighbor atom (labeled '7') also decrease. Although it is difficult to determine the actual distance when two Eu atoms are near each other in the z-direction, the fractions of both atoms 2 and 7 might have decreased in the experimental results as well.

By comparing analyzed and converted radial distribution functions, we can also demonstrate that the converted radial distribution functions are reasonable because of their agreement with the distribution shown in Fig. 7. While the radial distribution function of the real coordination system differs from the analyzed one, these two types of distributions nearly agree with the observed result. Therefore, except for the 2^{nd} and 7^{th} neighbor atoms, Eu atoms are almost randomly distributed in Ca-α-SiAlON. According to the STEM-HAADF analysis of Ca-doped α-SiAlON without Eu doping [36], a short-range Coulomb-like repulsive force exists between adjacent Ca atoms in the α-SiAlON network, in which the radial distribution function of Ca-Ca showed that the proportions of first and second nearest neighbor Ca atoms decrease, and the proportions of the third and fourth nearest neighbor atoms tend to increase. In the case of Eu atoms investigated in this study, the Ca concentration does not affect the Eu distribution. The decreased fraction of atoms 2 and 7 might be caused by the short-range

Coulomb-like repulsive forces. When two Eu or Ca atoms contact along x or y-direction, the Si atoms always locates between these atoms as shown in Fig.1, which decreases the interaction of these atoms owing to the screening effect. In contrast, the nitrogen or oxygen atoms are arranged between Ca or Eu atoms along the z-direction without Si atoms, which might enhance the short-range Coulomb-like repulsive forces. This is the reason for decreased fraction of atoms 2 and 7. Here, we must also consider the effects of the synthetic conditions on the dopant distribution, including temperature, time, and sintering or heat treatments. The reaction time for the combustion synthesis applied in this study was less than 5 min. The as-synthesized powder was observed without any heat treatment. In addition, the accuracy of through-focus HAADF-STEM is still low, especially for analyzing the fraction of atoms existing along the z-direction. In our future work, we will improve the accuracy of the through-focus method to analyze the distribution of Eu atoms in Ca-α-SiAlON.

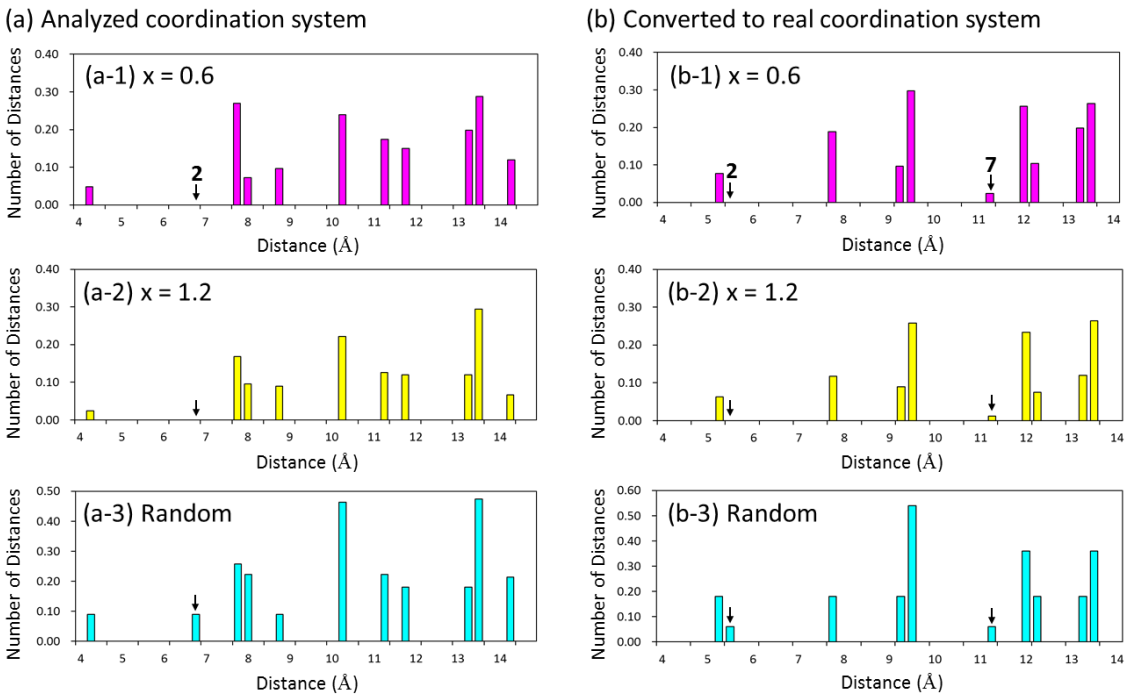

Fig. 8. Radial distribution functions of the analyzed coordination system (a) before and (b) after conversion to the real coordination system.

4. Conclusions

We have investigated the dopant distribution in Ca-α-SiAlON via through-focus HAADF-STEM imaging. Due to the shallow focus depth, the contrast of the dopant site changes as a function of the depths of nearby Eu atoms. Using a large convergence semi-angle greatly increases the depth resolution because the electron beam tends to spread instead of channeling along the atomic columns. Although the depth resolution of through-focus imaging is limited, a contrast depth profile with narrow step width was effective to determine the depths of Eu atoms with satisfactory accuracy. Finally, the resulting radial distribution function shows that the Ca concentration does not affect the Eu distribution and the decreased fraction of neighboring Eu atoms along z-direction might be caused by the enhanced short-range Coulomb-like repulsive forces along the z-direction compared to x or y-directions.

Acknowledgments

We thank Mr. Harada (Combustion Synthesis ltd.) for helping with materials synthesis. We gratefully acknowledge Mr. K. Ohkubo, Mr. R. Oota, Mr. T. Tanioka, Ms. Y. Yamanouchi and Ms. E. Obari for their technical support in TEM operations. This work was supported by Japan Society for the Promotion of Science KAKENHI (Grant Number 26249098). A part of this work was conducted at Hokkaido University and supported by the “Nanotechnology Platform” Program of the Ministry of Education, Culture, Sports, Science and Technology (MEXT), Japan.

References

[1] S. Nishiura, S. Tanabe, K. Fujioka, Y. Fujimoto, Properties of transparent Ce:YAG ceramic phosphors for white LED, Optical Materials, 33 (2011) 688-691.

[2] J.H. Ryu, Y.-G. Park, H.S. Won, S.H. Kim, H. Suzuki, J.M. Lee, C. Yoon, M. Nazarov, D.Y. Noh, B. Tsukerblat, Luminescent Properties of Ca- alpha -SiAlON:Eu[sup 2+] Phosphors Synthesized by Gas-Pressured Sintering, Journal of The Electrochemical Society, 155 (2008) J99-J104.
[3] K. Uheda, N. Hirosaki, Y. Yamamoto, A. Naito, T. Nakajima, H. Yamamoto, Luminescence Properties of a Red Phosphor, $CaAlSiN3:Eu2+$, for White Light-Emitting Diodes, Electrochemical and Solid-State Letters, 9 (2006) H22-H25.
[4] J.S. Kim, Y.H. Park, S.M. Kim, J.C. Choi, H.L. Park, Temperature-dependent emission spectra of M2SiO4:Eu2+ (M=Ca, Sr, Ba) phosphors for green and greenish white LEDs, Solid State Communications, 133 (2005) 445-448.
[5] R.-J. Xie, N. Hirosaki, M. Mitomo, T. Suehiro, X. Xu, H. Tanaka, Photoluminescence of Rare-Earth-Doped Ca-α-SiAlON Phosphors: Composition and Concentration Dependence, Journal of the American Ceramic Society, 88 (2005) 2883-2888.
[6] K. Sakuma, N. Hirosaki, R.J. Xie, Y. Yamamoto, T. Suehiro, Luminescence properties of (Ca,Y)-α-SiAlON:Eu phosphors, Materials Letters, 61 (2007) 547-550.
[7] Y. Chen, J. Xu, Y. Yu, W. Chen, R. Zeng, Preparation Eu-doped ca-α-SiAlON phosphor by heterogeneous precipitation: An orange–yellow phosphor for white light-emitting diodes, Ceramics International, 41 (2015) 11086-11090.
[8] R.-J. Xie, N. Hirosaki, M. Mitomo, Y. Yamamoto, T. Suehiro, K. Sakuma, Optical Properties of Eu2+ in α-SiAlON, The Journal of Physical Chemistry B, 108 (2004) 12027-12031.
[9] Y. Song, T. Masaki, K. Senthil, D. Yoon, Photoluminescence properties and synthesis of Eu2+-activated Ca-alpha-SiAlON phosphor for white LED application, JOURNAL OF CERAMIC PROCESSING RESEARCH, 14 (2013) S15-S17.
[10] J. Qiu, K. Miura, N. Sugimoto, K. Hirao, Preparation and fluorescence properties of fluoroaluminate glasses containing Eu2+ ions, Journal of Non-Crystalline Solids, 213–214 (1997) 266-270.
[11] K. Shioi, N. Hirosaki, R.-J. Xie, T. Takeda, Y.Q. Li, Y. Matsushita, Synthesis, Crystal Structure, and Photoluminescence of Sr-α-SiAlON:Eu2+, Journal of the American Ceramic Society, 93 (2010) 465-469.
[12] H. Rietveld, A profile refinement method for nuclear and magnetic structures, Journal of Applied Crystallography, 2 (1969) 65-71.
[13] T. Yamazaki, K. Watanabe, Y. Kikuchi, M. Kawasaki, I. Hashimoto, M. Shiojiri, Two-dimensional distribution of As atoms doped in a Si crystal by atomic-resolution high-angle annular dark field STEM, Physical Review B, 61 (2000) 13833-13839.
[14] S.I. Molina, D.L. Sales, P.L. Galindo, D. Fuster, Y. González, B. Alén, L. González, M. Varela, S.J. Pennycook, Column-by-column compositional mapping by Z-contrast imaging, Ultramicroscopy, 109 (2009) 172-176.

[15] A. Rosenauer, T. Mehrtens, K. Müller, K. Gries, M. Schowalter, P. Venkata Satyam, S. Bley, C. Tessarek, D. Hommel, K. Sebald, M. Seyfried, J. Gutowski, A. Avramescu, K. Engl, S. Lutgen, Composition mapping in InGaN by scanning transmission electron microscopy, Ultramicroscopy, 111 (2011) 1316-1327.
[16] P.M. Voyles, D.A. Muller, J.L. Grazul, P.H. Citrin, H.J.L. Gossmann, Atomic-scale imaging of individual dopant atoms and clusters in highly n-type bulk Si, Nature, 416 (2002) 826-829.
[17] N. Shibata, S.D. Findlay, S. Azuma, T. Mizoguchi, T. Yamamoto, Y. Ikuhara, Atomic-scale imaging of individual dopant atoms in a buried interface, Nat Mater, 8 (2009) 654-658.
[18] D.A. Muller, Structure and bonding at the atomic scale by scanning transmission electron microscopy, Nat Mater, 8 (2009) 263-270.
[19] C.-L. Jia, J. Barthel, F. Gunkel, R. Dittmann, S. Hoffmann-Eifert, L. Houben, M. Lentzen, A. Thust, Atomic-Scale Measurement of Structure and Chemistry of a Single-Unit-Cell Layer of LaAlO3 Embedded in SrTiO3, Microsc. Microanal., 19 (2013) 310-318.
[20] N. Shibata, S.J. Pennycook, T.R. Gosnell, G.S. Painter, W.A. Shelton, P.F. Becher, Observation of rare-earth segregation in silicon nitride ceramics at subnanometre dimensions, Nature, 428 (2004) 730-733.
[21] L. Gan, F.-F. Xu, X.-H. Zeng, Z.-S. Li, Z.-Y. Mao, P. Lu, Y.-C. Zhu, X.-J. Liu, L.-L. Zhang, Multiple doping structures of the rare-earth atoms in [small beta]-SiAlON:Ce phosphors and their effects on luminescence properties, Nanoscale, 7 (2015) 11393-11400.
[22] T. Takeda, N. Hirosaki, R.-J. Xie, K. Kimoto, M. Saito, Anomalous Eu layer doping in Eu, Si co-doped aluminium nitride based phosphor and its direct observation, Journal of Materials Chemistry, 20 (2010) 9948-9953.
[23] K. Kimoto, R.-J. Xie, Y. Matsui, K. Ishizuka, N. Hirosaki, Direct observation of single dopant atom in light-emitting phosphor of β-SiAlON:Eu²⁺, Applied Physics Letters, 94 (2009) N.PAG.
[24] F. Xu, E. Sourty, W. Shi, X. Mou, L. Zhang, Direct Observation of Rare-Earth Ions in α-Sialon:Ce Phosphors, Inorganic Chemistry, 50 (2011) 2905-2910.
[25] M.C. Scott, C.-C. Chen, M. Mecklenburg, C. Zhu, R. Xu, P. Ercius, U. Dahmen, B.C. Regan, J. Miao, Electron tomography at 2.4-angstrom resolution, Nature, 483 (2012) 444-447.
[26] D. Van Dyck, F.-R. Chen, /`Big Bang/' tomography as a new route to atomic-resolution electron tomography, Nature, 486 (2012) 243-246.
[27] S. Van Aert, K.J. Batenburg, M.D. Rossell, R. Erni, G. Van Tendeloo, Three-dimensional atomic imaging of crystalline nanoparticles, Nature, 470 (2011) 374-377.

[28] K. Inoue, F. Yano, A. Nishida, H. Takamizawa, T. Tsunomura, Y. Nagai, M. Hasegawa, Dopant distributions in n-MOSFET structure observed by atom probe tomography, Ultramicroscopy, 109 (2009) 1479-1484.
[29] S. Du, T. Burgess, B. Gault, Q. Gao, P. Bao, L. Li, X. Cui, W. Kong Yeoh, H. Liu, L. Yao, A.V. Ceguerra, H. Hoe Tan, C. Jagadish, S.P. Ringer, R. Zheng, Quantitative dopant distributions in GaAs nanowires using atom probe tomography, Ultramicroscopy, 132 (2013) 186-192.
[30] M. Bar-Sadan, J. Barthel, H. Shtrikman, L. Houben, Direct Imaging of Single Au Atoms Within GaAs Nanowires, Nano Lett., 12 (2012) 2352-2356.
[31] R. Ishikawa, A.R. Lupini, S.D. Findlay, S.J. Pennycook, Quantitative Annular Dark Field Electron Microscopy Using Single Electron Signals, Microsc. Microanal., 20 (2014) 99-110.
[32] J.M. LeBeau, S.D. Findlay, L.J. Allen, S. Stemmer, Standardless Atom Counting in Scanning Transmission Electron Microscopy, Nano Lett., 10 (2010) 4405-4408.
[33] R. Ishikawa, A.R. Lupini, S.D. Findlay, T. Taniguchi, S.J. Pennycook, Three-Dimensional Location of a Single Dopant with Atomic Precision by Aberration-Corrected Scanning Transmission Electron Microscopy, Nano Lett., 14 (2014) 1903-1908.
[34] J. Hwang, J.Y. Zhang, A.J. D'Alfonso, L.J. Allen, S. Stemmer, Three-Dimensional Imaging of Individual Dopant Atoms in ${¥mathrm{SrTiO}}_{3}$, Phys. Rev. Lett., 111 (2013) 266101.
[35] J.Y. Zhang, J. Hwang, B.J. Isaac, S. Stemmer, Variable-angle high-angle annular dark-field imaging: application to three-dimensional dopant atom profiling, Scientific Reports, 5 (2015) 12419.
[36] N. Sakaguchi, F. Yamaki, G. Saito, Y. Kunisada, Estimating the dopant distribution in Ca-doped α-SiAlON: statistical HAADF-STEM analysis and large-scale atomic modeling, Microscopy, (2016).
[37] A.Y. Borisevich, A.R. Lupini, S.J. Pennycook, Depth sectioning with the aberration-corrected scanning transmission electron microscope, Proc. Natl. Acad. Sci. U.S.A., 103 (2006) 3044-3048.
[38] A.Y. Borisevich, A.R. Lupini, S. Travaglini, S.J. Pennycook, Depth sectioning of aligned crystals with the aberration-corrected scanning transmission electron microscope, J. Electron Microsc., 55 (2006) 7-12.
[39] S. Wang, A.Y. Borisevich, S.N. Rashkeev, M.V. Glazoff, K. Sohlberg, S.J. Pennycook, S.T. Pantelides, Dopants adsorbed as single atoms prevent degradation of catalysts, Nat Mater, 3 (2004) 143-146.

[40] K. van Benthem, A.R. Lupini, M. Kim, H.S. Baik, S. Doh, J.-H. Lee, M.P. Oxley, S.D. Findlay, L.J. Allen, J.T. Luck, S.J. Pennycook, Three-dimensional imaging of individual hafnium atoms inside a semiconductor device, Appl. Phys. Lett., 87 (2005) 034104.
[41] E.C. Cosgriff, P.D. Nellist, A Bloch wave analysis of optical sectioning in aberration-corrected STEM, Ultramicroscopy, 107 (2007) 626-634.
[42] G. Saito, J. Niu, X. Yi, Y. Kunisada, N. Sakaguchi, T. Akiyama, Salt-assisted combustion synthesis of Ca-α-SiAlON:Eu2+ phosphors, J. Alloys Compd., 681 (2016) 22-27.
[43] J. Niu, G. Saito, T. Akiyama, A New Route to Synthesize β-SiAlON:Eu 2+ Phosphors for White Light-Emitting Diodes, Applied Physics Express, 6 (2013) 042105.
[44] J. Barthel, Dr. Probe-STEM simulation software, http://www.er-c.org/barthel/drprobe/, in.
[45] A. Weickenmeier, H. Kohl, Computation of absorptive form factors for high-energy electron diffraction, Acta Crystallogr. Sect. A: Found. Crystallogr., 47 (1991) 590-597.
[46] Y. Oshima, Y. Hashimoto, Y. Tanishiro, K. Takayanagi, H. Sawada, T. Kaneyama, Y. Kondo, N. Hashikawa, K. Asayama, Detection of arsenic dopant atoms in a silicon crystal using a spherical aberration corrected scanning transmission electron microscope, Physical Review B, 81 (2010) 035317.

Figure captions

Fig. 1. (a) Atomic structure model of Eu-doped Ca-α-SiAlON, in the [0001] direction. (b) Multi-slice simulated image of Eu-doped Ca-α-SiAlON, in which one Eu atom is located at -5.48 nm along the z-direction and defocus is -5.52 nm (sample thickness: 20 nm, convergence semi-angle: 30 mrad).

Fig. 2. (a) Simulated images of an Eu site with different levels of defocus from 0.00 to -11.04 nm. (b, c) defocus profiles of an Eu site evaluated via multi-slice simulation with different electron probe convergence semi-angles, and different depth positions of Eu atoms.

Fig. 3. Defocus profiles via multi-slice image simulation with two Eu atoms located at different depths of (a) -5.48 and -10.62 nm, and (b) -5.48 and -7.19 nm.

Fig. 4. HAADF-STEM images at different defocus values of Eu doped Ca-α-SiAlON of x = 0.6 No. 1 (a) and No. 2 (b) with averaged HAADF-STEM images, which are the averages of 30 images obtained at different defocus values. (c) Enlargement of column c in Fig. 4(a) at each defocus level (nm).

Fig. 5. Contrast profiles acquired from through-focus HAADF-STEM images of Eu-doped Ca-α-SiAlON (x=0.6), in which (a-d) correspond to the arrows in Figs. 4(a, b).

Fig. 6. 3D Eu atom distributions for (a) x=0.6 and (b) x=1.2.

Fig. 7. (a) Real coordination system of Eu sites and (b) simulated coordination system and its corresponding radial distribution functions.

Fig. 8. Radial distribution functions of the simulated coordination system (a) before and (b) after conversion to the real coordination system.